

Wafer-Scale Fabrication of Single Domain Magnetic Nanostructures

2023 CNF REU Intern: Naomi Sharlotte Naranjo

Intern Affiliation: Mechanical Engineering, Cornell University

CNF REU Principal Investigator: Professor Itai Cohen; Physics, Cornell University

CNF REU Mentors: Melody Xuan Lim, Zexi Liang; Physics, Cornell University

Program & Primary Source of Research Funding: 2023 Cornell NanoScale Facility Research Experiences for Undergraduates (CNF REU) Program via the National Science Foundation under Grant No. NNCI-2025233

Contact: nsn25@cornell.edu, itai.cohen@cornell.edu, mxl3@cornell.edu, zl467@cornell.edu

Website(s): <https://cnf.cornell.edu/education/reu/2023>

Primary CNF Tools Used: ASML DUV Stepper, Oxford 82, Gamma Automatic Coat-Develop Tool, SEM, AFM, P7 Profilometer

Abstract:

Single-domain magnets are critical to the development of untethered micromachines. To achieve single-domain behavior, these magnets must have a width of under 100 nanometers (nm). The current fabrication method of these magnets, electron-beam lithography, is both time and cost consuming. To address this, we developed a process to use Deep Ultraviolet (DUV) lithography as a more accessible alternative to the e-beam lithography process. Through precise etching of chromium on quartz photomasks, we can produce phase-shift photomasks with a 180-degree phase-shift, allowing for greater pitch density and depth of focus. Further improvements to the feature width in photoresist can be made by optimizing parameters on the ASML DUV Stepper. Our process successfully created features with a range of widths under the 100 nm threshold. Additionally, we characterized the optimal doses to achieve pitches ranging from 400 to 300 nm and control over the spacing between features.

Summary of Research:

Phase-shift photomasks are fully quartz masks with features etched to a specified depth such that there is a 180-degree phase shift of the light that passes through the etched area. This allows the light intensity to drop to zero at the boundary between the two different depth areas on the mask, leading to two features being defined on the wafer for each feature on the mask, increasing feature density and giving a larger process window.

The phase-shift mask fabrication process involved first using the Heidelberg Mask Writer DWL2000 to write a chrome on quartz mask and then using the CHF_3/O_2 oxide etching recipe on the Oxford 82 etcher to etch the quartz on the mask to a desired depth of 248 nm. The etching process consisted of etching the mask for an initial five minutes and using the P7 Profilometer to calculate the chrome and quartz etching rates and remaining etch time. Once the final depth was reached, the chrome was etched

off the mask and the final quartz depth was verified using an atomic force microscope (AFM).

Each image on the phase shift mask consisted of vertical alternating etched and unetched lines that were 100 μm long, with pitches ranging from 400 to 800 nm. Within each pitch, there were biases added to the width of the etched area, such that without bias the width of the etched and unetched lines were equal and with a positive bias the width of the etched line is greater than the unetched line while keeping the same pitch. This image was arranged into a 5×7 array on the mask, and S1813 photoresist was used to cover alignment marks and other features on the mask while etching one column of the array at a time.

The images were exposed on 4-inch wafers, that were coated with 62 nm of anti-reflective coating (ARC) and 300 nm of DUV210 photoresist using the Gamma Automatic Coat-Develop Tool. On the ASML DUV Stepper, the numerical aperture was set to 0.63, the illumination mode was set to partial coherent with an outer sigma of 0.302 and the focus was $-0.1 \mu\text{m}$, these parameters were shown to give the best results for phase-shift masks on a simulation software called Prolith. The cell size was set to 10 mm in order to fit multiple cells into a matrix on the wafer, which allowed a range of doses from 6 mJ/cm^2 to 21 mJ/cm^2 to be tested.

Scanning electron microscopy (SEM) was used to analyze the results of the exposures. SEM imaging showed that there was a range of line widths under the 100 nm target and that the line widths decreased as the dose increased (see Figure 1). Two distinct spacings between the lines were also observed, with one spacing being usually larger than the other. The ratio of these spacings was characterized at each of the biases tested on the mask (see Figure 2), which showed that as the unetched area becomes larger than the etched area, the spacing between the lines becomes more equal. This trend supports the hypothesis that the lines are falling onto the area that

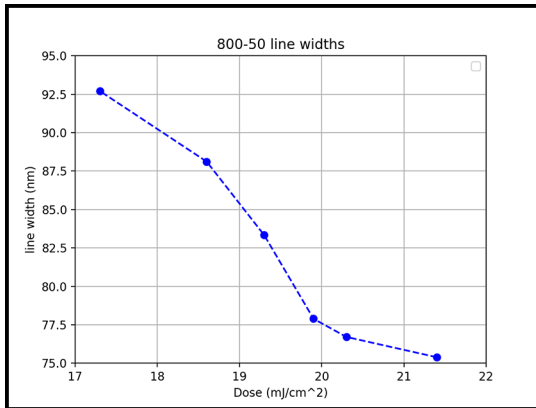


Figure 1: Line width of 800 pitch with a negative 50 bias across various doses.

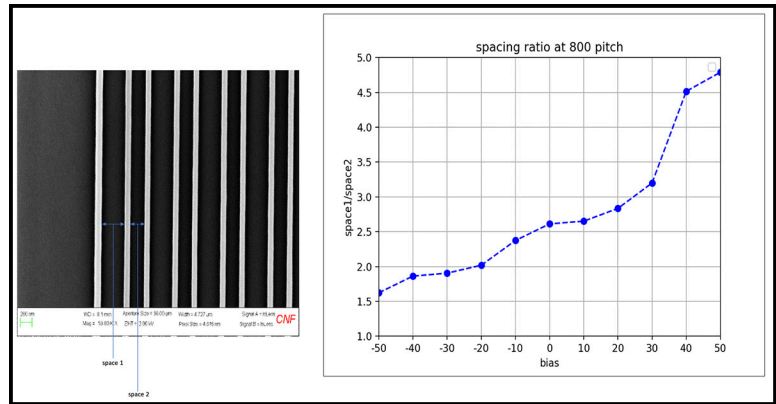


Figure 2: Ratio of line spacings at 800 nm pitch at 18.6 mJ/cm² dose across various biases.

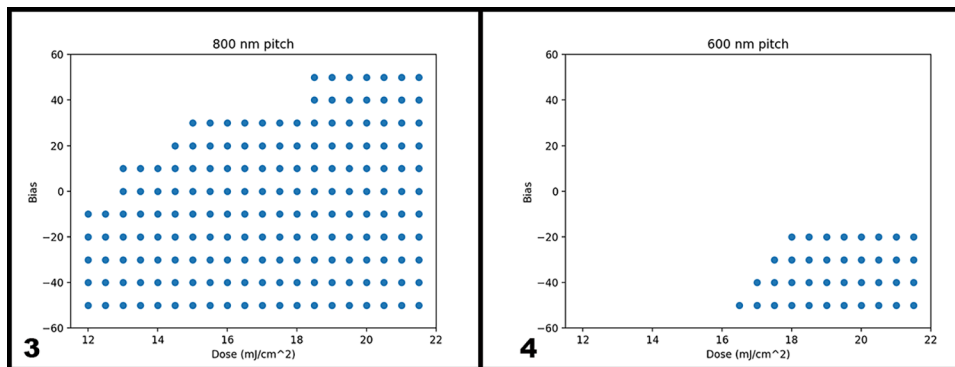


Figure 3, left: Process window for 800 nm pitch. Figure 4, right: Process window for 600 nm pitch.

is unetched on the mask, so the unetched area must be greater than the etched area for the spacing to be uniform. The largest negative bias tested was 50 nm, which lead to a ratio of 1.5, so the ideal negative bias should be greater.

The highest pitch tested was 800 nm on the mask, which translates to 400 nm on the wafer. This pitch had the largest process window (see Figure 3), working at all the doses tested and all the biases. Pitches of 700 nm and 600 nm on the mask were also achieved, but as the pitch decreased, the process window shrunk to higher doses and greater negative biases (see Figure 4). Some pitch doubling was seen at 500 nm, but it was not uniform throughout the length of the lines. However, with a greater negative bias, the photoresist could possibly be fully exposed between the lines making the 500 nm pitch better defined.

Conclusions and Future Steps:

We demonstrated that we could fabricate a phase-shift mask completely at the CNF with an etch depth less than 10 nm away from our target of 248 nm. Using said mask, we achieved features with a range of widths less than 100 nm and were able to control the line width through changes in dose. We also were able to characterize the spacing between the lines and understand how to use bias on our mask to get uniform spacing.

Acknowledgements:

Special thanks to the Cornell NanoScale Facility Research Experiences for Undergraduates (CNF REU) Program for hosting this internship, and to the Cohen Research Group for their support and mentorship. This work was funded by the National Science Foundation via grant no. NNCI-2025233.

Electrical Characterization of Dielectric Films

2023 CNF iREG Intern: Toko Ogata

Intern Affiliation: Chemistry, Graduate School of Chemical Sciences and Engineering, Hokkaido University, Hokkaido, Japan

CNF iREG Principal Investigator: Dr. Lynn Rathbun, Cornell NanoScale Facility (CNF), Cornell University

CNF iREG Mentors: Jeremy Clark, Phil Infante, Aaron Windsor; CNF, Cornell University

Program & Primary Sources of Research Funding: 2023 Cornell NanoScale Facility International Research Experiences for Graduates (CNF iREG) Program via the NSF under Grant No. NNCI-2025233; NNCI/NIMS Graduate Exchange Fellowship Program administered by Coordination Office, Center of Advanced Research Infrastructure for Materials and Nanotechnology of the National Institute for Materials Science - NIMS

Contact: carnation@eis.hokudai.ac.jp, rathbun@cnf.cornell.edu,

clark@cnf.cornell.edu, infante@cnf.cornell.edu, windsor@cnf.cornell.edu

Website(s): <https://cnf.cornell.edu/education/reu/2023>, <https://nanonet.mext.go.jp/page/NNCI-prg.html>

Primary CNF Tools Used: SC4500 Even-Hour Evaporator, Keithley 4200A - IVCV Testing Station, Arradiance ALD Gemstar-6, MOS Metal Anneal 3 - C1

Abstract:

The characteristics of dielectric thin films have been studied to improve the performance and sizing of semiconductor devices, especially Metal-Oxide-Semiconductor Field Effect Transistors (MOSFETs). The MOSFET switches the current flow by inversion on the semiconductor surface as applied voltage across the MOS capacitor. The MOS capacitor is the heart of the MOSFET, because the operation and characterization are dependent on this inversion. Since the performance of the MOS capacitor is strongly affected by the properties of the oxide film, different dielectric materials and deposition tools are expected to have different C-V curves. We compared the C-V curves of devices using different deposition tools and materials, then discussed which is the best to fabricate MOS capacitors.

Summary of Research:

The Metal-Oxide-Semiconductor Field Effect Transistor (MOSFET) is a three-terminal device, called Gate, Drain, and Source, used for amplifying or switching electronic signals. When the proper voltage is applied to the gate, the semiconductor surface at the interface of oxide and semiconductor is inverted from n-type to p-type or from p-type to n-type, depending on the semiconductor substrate used. The current flows between source and drain. This Metal-Oxide-Semiconductor structure applied the gate voltage known as MOS Capacitor. The MOS capacitor is the heart of MOSFET.

The capacitance of the MOS capacitor changes by sweeping the gate voltage. The Capacitance-Voltage (C-V) characteristic curve provides some useful information. The C-V curves visualize three regimes of the MOS capacitor: Accumulation, Depletion, and Inversion. The

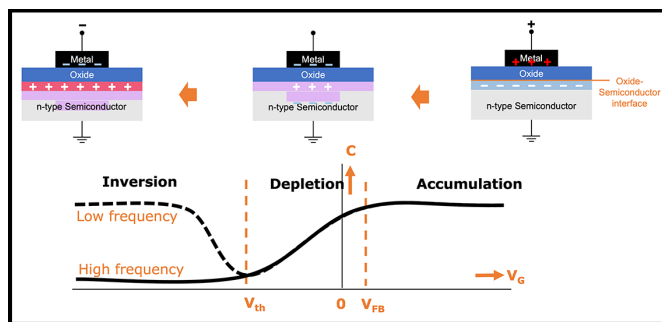


Figure 1: The schematic of the C-V curve for the n-type MOS capacitor at low frequency voltage (dashed), and high frequency voltage (solid) and three regimes: Accumulation regime (right part), Depletion regime (center part), and Inversion regime (left part).

voltages at boundaries of regions are called Flat-band Voltage (V_{FB}) and Threshold Voltage (V_{th}), respectively. V_{FB} is defined as the voltage such that there is zero net charge density in oxide material, and V_{th} as the minimum voltage required to create an inversion layer. These are one of the most important parameters that can be extracted from C-V curves. Since the characteristics of the MOS device is strongly affected by the oxide films, the C-V curve also gives properties of oxide films such as the permittivity. Figure 1 shows the schematic of the C-V curve for the n-type MOS capacitor.

Therefore, we measured the C-V curve for device characterization, and compared the differences in deposition tools and materials, to find which is the best to fabricate MOS capacitors. MOS capacitors, consisting of an aluminum electrode, a dielectric film of various

materials, and a n-type silicon substrate body, were made by a simple process: 20-50 nm silicon dioxide (SiO_2), hafnium oxide (HfO_2), zirconium dioxide (HfO_2), and aluminum oxide (Al_2O_3) films were formed on the n-type silicon wafer, then 200 nm of aluminum was deposited through a shadow mask. Various tools were used to deposit SiO_2 films, including High-Density Plasma Chemical Vapor Deposition (HDP-CVD), e-beam evaporators, and thermal oxidation. For depositing other dielectric films, we used Atomic Layer Deposition (ALD). The fabricated devices were evaluated by measuring and analyzing Capacitance-Voltage (C-V) characteristics at various frequencies. We performed 5% H_2/N_2 anneal to improve the interface trap for getting a better C-V curve. The thickness of oxide films is measured by a variable angle ellipsometer.

First, we compared the normalized C-V curves of the MOS device with SiO_2 film deposited by different tools at various frequencies (Figure 2). The C-V results are different between deposition tools, such as threshold voltage, flat-band voltage, frequency dependence. We observed the sharp transition from accumulation to inversion, so it can be said that evaporator and dry oxidation are great tools for device fabrication.

Next, we compared the normalized C-V curves of the MOS device with different dielectric films at various frequencies (Figure 3, Figure 4). The shape of C-V curves is widely different between materials. Since there is a leakage from Al_2O_3 films, we considered Al_2O_3 is a bad dielectric. The C-V curves for SiO_2 and HfO_2 clearly show sharp transitions with small frequency dependence. SiO_2 and HfO_2 are great for MOS capacitors, in addition, ALD is also a great tool for fabrication.

Conclusions and Future Steps:

From the C-V curves, we conclude that e-beam evaporator, dry oxidation, and ALD are great tools for fabrication of the MOS capacitors. SiO_2 , HfO_2 are great materials for the MOS capacitor, but Al_2O_3 is a bad dielectric. For the next step, we will consider using other tools, dielectric materials, and gate electrode metals for comparison. To get better results, we will optimize some deposition conditions and measurement parameters including deposition temperature, thickness, and delay time for sweep.

Acknowledgements:

I would like to express my appreciation to my PI Dr. Lynn Rathbun, my mentors Jeremy Clark, Phil Infante, and Aaron Windsor for the advice on experimental design and useful discussion. This work is supported by National Science Foundation under Grant No. NNCI-2025233, National Nanotechnology Coordinated Infrastructure, Cornell NanoScale Science & Technology Facility, Center of Advanced Research Infrastructure for Materials and Nanotechnology of NIMS.

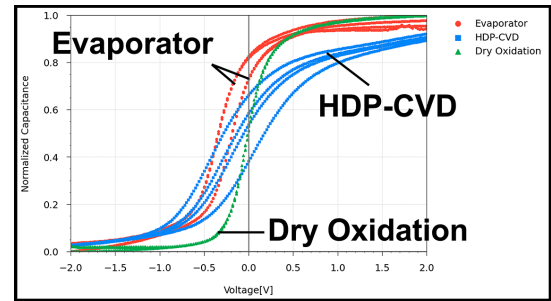


Figure 2: The C-V curves at 10 kHz, 20 kHz, 30 kHz, and 100 kHz for 46.84 nm SiO_2 deposited by the e-beam evaporator (red circle), 42.94 nm SiO_2 deposited by HDP-CVD (blue square), and 19.13 nm SiO_2 formed by dry oxidation (green triangle).

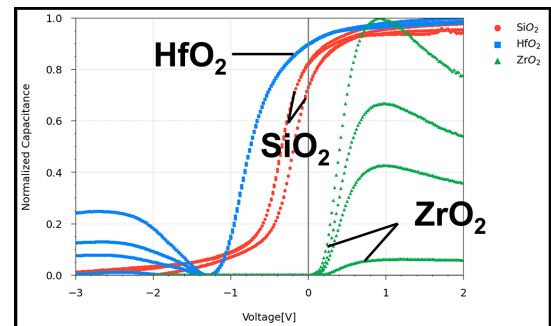


Figure 3: The C-V curves at 10 kHz, 20 kHz, 30 kHz, and 100 kHz for 46.84 nm SiO_2 deposited by the e-beam evaporator (red circle), 44.99 nm HfO_2 deposited by ALD (blue square), and 11.04 nm ZrO_2 deposited by ALD (green triangle).

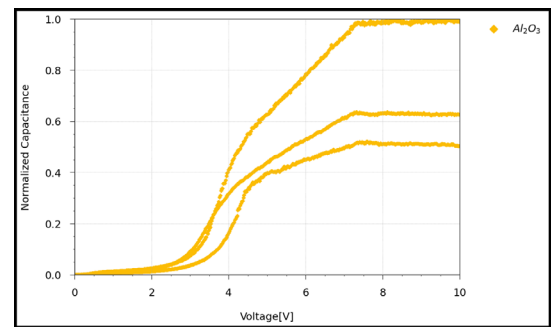


Figure 4: The C-V curves at 10 kHz, 20 kHz, 30 kHz, and 100 kHz for 32.61 nm Al_2O_3 deposited by ALD (yellow diamond).

References:

- [1] Houssa, Michel, et al. "Electrical properties of high- κ gate dielectrics: Challenges, current issues, and possible solutions." *Materials Science and Engineering: R: Reports* 51.4-6 (2006): 37-85.
- [2] Wang, Yichun, "Leakage current reduction of MOS capacitor induced by rapid thermal processing" (2010). University of Kentucky Master's Theses 640. https://uknowledge.uky.edu/gradschool_theses/640.

Nanoimprint Process Optimization for PMMA

2023 CNF REU Intern: Amara Taddeo

Intern Affiliation: Chemistry, Allegheny College

2023 CNF REU Mentors: Roberto Ricardo Panepucci, Xinwei Wu; Cornell NanoScale Facility, Cornell University Program & Primary Source of Research Funding: 2023 Cornell NanoScale Facility Research Experiences for

Undergraduates (CNF REU) Program via the National Science Foundation under Grant No. NNCI-2025233

Contact: maratad283@gmail.com, rrp23@cornell.edu, wu@cornell.edu

Website(s): <https://cnf.cornell.edu/education/reu/2023>, <https://www.cnfusers.cornell.edu/node/43>

Primary CNF Tools Used: Nanoimprint NX-2500, P7 Profilometer, Oxford 81/82, MVD100, AFM, SEM

Abstract:

Nanoimprint lithography (NIL) has the capabilities of having high resolution, producing features that are sub-10-nm and is also cost-effective compared to lithography techniques with same resolution, such as electron-beam lithography. To achieve such benefits, nanoimprinting parameters must be optimized, such as imprint temperature, pressure, polymer physical properties, residual layer thickness, and etch depth of mask, among others. Within the parameters explored, optimal thermal nanoimprint lithography (T-NIL) guidelines were achieved with polymethyl methacrylate (PMMA), a well-understood electron-beam resist, on Si wafers on the Nanonex NX-2500 with one non-uniform density pattern and a uniform grating pattern. For widest pattern conditions, optimal T-NIL parameters occurred around 250°C with an imprint time of 210 seconds using 50K PMMA, for a 180 nm deep mask.

Summary of Research:

While there are many factors that affect the optimization of nanoimprint lithography, a crucial factor is the temperature of imprint. To achieve an optimal imprint, the polymer needs to be in a viscous state where it can flow completely into the desired pattern being imprinted. For an optimal temperature to achieve such a polymer state, the glass transition temperature, T_g , needs to be taken into consideration [1]. Optimal imprinting begins approximately 70°C to 80°C above T_g so that the polymer is not just in a rubbery state but in a viscous state [1,2]. As for polymethyl methacrylate (PMMA), PMMA has a T_g of approximately 105°C [1]. Therefore, an ideal imprint temperature was determined to be 250°C for a pressure of 200 PSI.

PMMA comes in varying molecular weights such as 950K, 495K, and 50K, each with different polymer chain lengths with 950K PMMA having the longest and 50K PMMA having the shortest. In Figure 1, with an imprint time of 210s, both 50K and 495K PMMA have adequate imprints while 950K PMMA is still not ideal.

UV exposure was considered for enhancement, because when PMMA is irradiated, scissions occur within the polymer chains, reducing the average molecular weight [3]. With polymer chain scissions, the T_g is affected, enhancing nanoimprinting conditions. A wafer with 950K PMMA was flood exposed at $\lambda_{UV} = 220$ nm with 12 mW/cm² UV followed by an imprint time of 120s, and the results are shown in Figure 1. There is a significant increase in the percent filled compared to the 950K PMMA with no UV exposure imprinted for longer time. Figure 2 exemplifies a typical defect with non-ideal imprinting parameters; PMMA filled in half of the width of the line, not filling completely into the pattern on the mask. Figure 3 shows a scanning electron microscope (SEM) image after Si RIE etching of a PMMA nanoimprinted pattern. The image highlights two problems that must be avoided, specifically, incomplete removal of the residual layer, and complete removal of the PMMA mask during RIE etching. Roughness in the bottom surface was due to incomplete residual layer etching in O₂ plasma of the PMMA, prior to the full SF₆ RIE etch. Complete removal of the PMMA mask due to poor selectivity led to further roughness on the top surface of the structures on the final stages of the Si etch.

A uniform grating pattern with a pitch of 800 nm and trenches with sizes of 541 nm was also explored. Figure 4 is a SEM image of a typical area after optimal nanoimprinting with 200 PSI, 250°C, and for 210s on an 82 nm PMMA coated wafer. While there were large areas that were imprinted fully, some defects were found over some portions of the sample.

Conclusions and Future Steps:

In the parameter space explored in this research, optimal nanoimprinting for non-uniform density patterns for PMMA on Si wafers were determined. These conditions require a temperature of at least 250°C with a pressure of 200 PSI. Print time for 100-400 nm layer thicknesses of 50K PMMA can be 120s for feature sizes from 5 μm

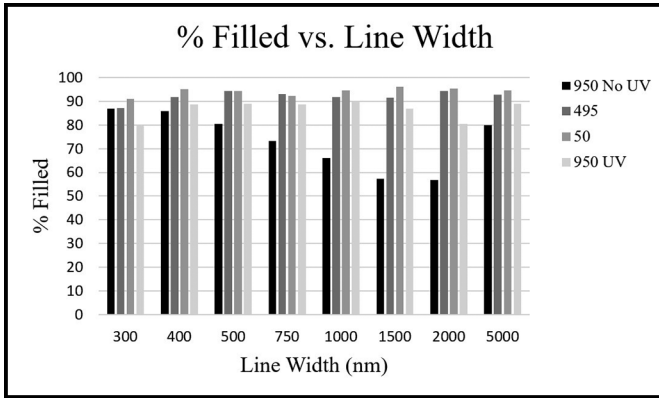


Figure 1: Graph comparing the percent of imprint pattern filled for varying molecular weights of PMMA along with prior UV exposure before imprinting for 950 PMMA for each line width of a non-uniform pattern.

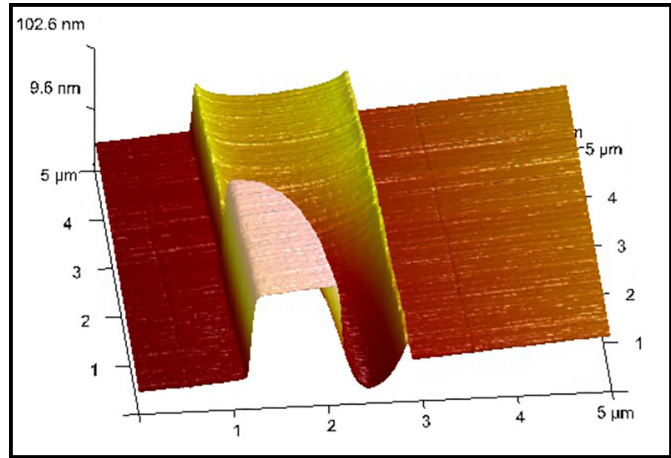


Figure 2: AFM image of a common partially filled line after nanoimprinting is done at not optimized parameters.

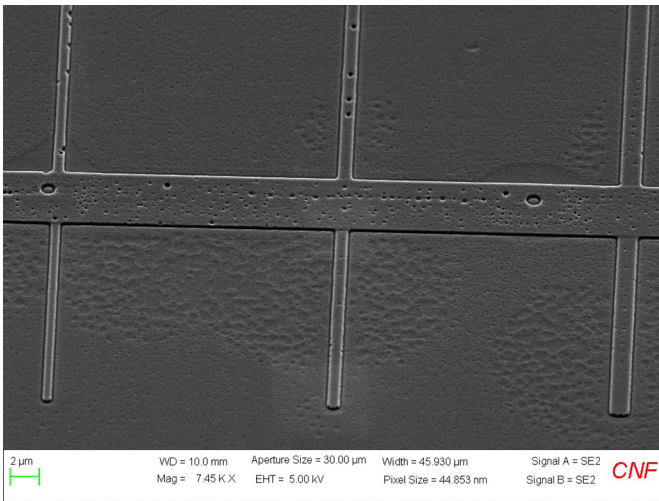


Figure 3: SEM image of after pattern transfer through RIE. Roughness on bottom was due to incomplete residual layer etch.

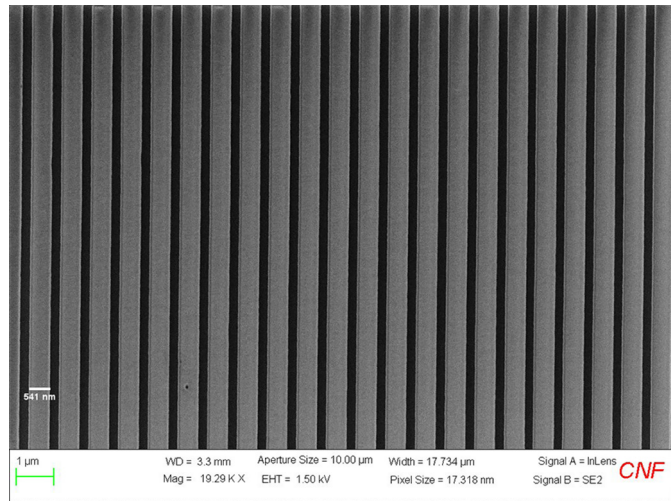


Figure 4: SEM image of a uniform grating pattern after being imprinted with a pitch of 800 nm and feature sizes of 541 nm.

to 300 nm, while 210s is required for 495K PMMA layers. For optimal printing at 950K PMMA, we have determined that 12 mW of UV at $\lambda = 220$ nm for 6s leads to optimal patterning. Uniform printing of the grid pattern was achieved over large areas; however, some areas of the wafer still contained non-uniformities within the pattern. Additional work is required to reproduce large features above $20 \mu\text{m}$. We plan to explore printing with 50K PMMA with UV exposure. Furthermore, careful consideration must be given to the depth of pattern transfer during the nanoimprint etch steps, due to PMMA being a poor mask in reactive ion corrosion (RIE).

Acknowledgements:

Special thanks to the Cornell NanoScale Facility Research Experiences for Undergraduates (CNF REU)

Program for hosting this internship and to the CNF staff for their support and mentorship. This work was funded by the National Science Foundation via grant no. NNCI-2025233.

References:

- [1] L.J. Guo, "Recent progress in nanoimprint technology and its applications," *Journal of Physics D: Applied Physics* 37(11), (2004).
- [2] R.N. Li, F. Chen, C.H. Lam, and O.K.C. Tsui, "Viscosity of PMMA on silica: Epitome of systems with strong polymer-substrate interactions," *Macromolecules* 46(19), 7889-7893 (2013).
- [3] J.O. Choi, "Degradation of poly(methylmethacrylate) by deep ultraviolet, x-ray, electron beam, and proton beam irradiations," *Journal of Vacuum Science & Technology B: Microelectronics and Nanometer Structures* 6(6), 2286 (1988).

Wafer Scale Piezoelectric Transformers

CNF Project Number: 1121-03

Principal Investigator(s): Prof. Amit Lal

User(s): Meera Vikas Garud

Affiliation(s): Electrical and Computer Engineering, Cornell University

Primary Source(s) of Research Funding: ARPA-E

Contact: amit.lal@cornell.edu, mvg44@cornell.edu

Website(s): <https://sonicmems.ece.cornell.edu/>

Primary CNF Tools Used: Westbond 7400A Ultrasonic Wire Bonder

Abstract:

Our project aims at developing a wafer scale-wafer mountable piezoelectric transformer for a wafer scale, compact ion accelerator. Miniaturizing conventional magnetic transformers is often a difficult task. However, piezoelectric transformer designs offer a promising alternative by utilizing the vibrational mode shapes of piezoelectric plates to achieve voltage gain. Various modes of vibration, such as shear-transverse, radial, and others, have been explored using different plate geometries. In our research, we aim to tackle the challenge by combining multiple approaches. We design a piezoelectric transformer that utilizes mechanical resonance of the structure, employs multilayer stacking, and incorporates a series electrical connection on the secondary side of the transformer. The device's design is specifically optimized for easy manufacturing and chip-scale assembly onto a PCB board, enhancing its practicality and potential for widespread adoption.

Summary of Research:

We use high Q fused quartz as a substrate and PZT pieces as the piezoelectric material. Figure 1 and Figure 2 illustrate the schematic and photograph of the device stack. The transformer consists of a 200 μm thick PZT layer, a 500 μm thick fused quartz layer, and three PZT pieces connected in series on the secondary side. To manufacture this transformer, we employ the LPKF laser cutter to obtain PZT pieces of the required area, and we use patterned copper tape as the metal contact on both sides of the transformer. We achieve the series connection at the secondary side PZT pieces using wire-bonds. The aluminum wire of the wire bonder is compatible with the sintered nickel metal layer on the PZT pieces. The wire bonds aid in electrical connections without shifting the resonance frequency due to the mass loading effect on the PZT pieces.

Conclusions and Future Steps:

The prototype gives promising results. We achieve a voltage gain of 6 at 8 MHz from a very thin ($<1\text{mm}$) device. To avoid effects of a non-uniform adhesion between PZT pieces and the copper tape on the frequency response, we propose the use of indium plating and flip-chip bonding to have better process control — for which Pico MA FinePlacer FlipChip Bonder would be a useful tool at CNF, and process flow would be modified appropriately. This will also aid in precise alignment of secondary side small PZT pieces with respect to the primary side larger PZT actuator.

References:

- [1] Y. Hou et al., "Vertically Stacked Piezoelectric Transformer for High Frequency Power Amplifier," 2023 IEEE Applied Power Electronics Conference and Exposition (APEC), Orlando, FL, USA, 2023, pp. 392-396.
- [2] M. Garud, Y. Hou, A. Lal, K. Afridi, "Piezoelectric Transformer using bulk PZT & Fused Quartz for RF Ion Accelerators," in 2023 IEEE International Ultrasonics Symposium (IUS), 2023.

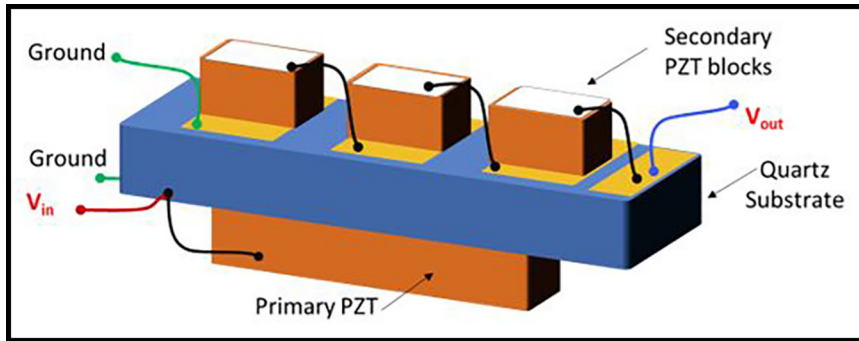


Figure 1: Schematic of the piezoelectric transformer architecture.

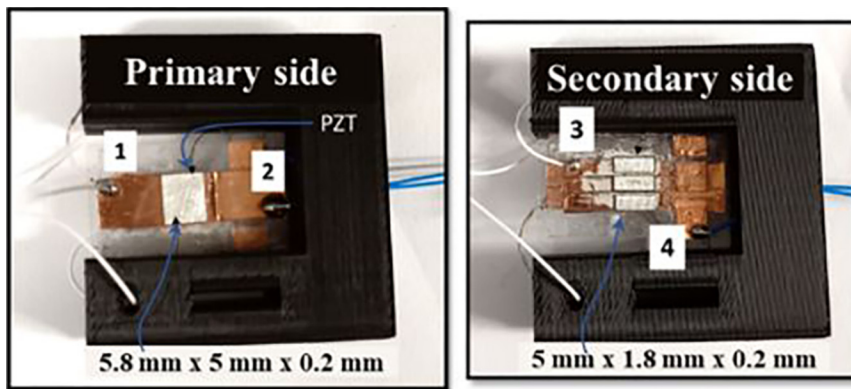


Figure 2: Photograph of a prototype of the transformer mounted on a 3D printed support structure.

Exploring the Relevance of Mucin-Induced Extracellular Vesicles in Therapeutics and Cancer

CNF Project Number: 2272-14

Principal Investigator(s): Dr. Matthew Paszek

User(s): Erik Chow

Affiliation(s): Department of Biomedical Engineering, Cornell University

Primary Source(s) of Research Funding: National Science Foundation Graduate Research Fellowship

Contact: paszek@cornell.edu, ec829@cornell.edu

Primary CNF Tools Used: Malvern NS300 Nanosight

Abstract:

Extracellular vesicles (EVs) have garnered increasing biomedical research focus due to their ability to transport DNA, RNA, and proteins. In a therapeutic context, EVs represent inherently biocompatible vessels for targeted delivery. However, in a disease context such as cancer, EVs become an avenue for disease pathogenesis and progression. In either context, the significance of the glycocalyx in EV biogenesis and function is largely unexplored, and the capacity to effect EV production and properties through rational manipulation of the glycocalyx remains poorly understood. We have previously demonstrated that overexpressing the mucin glycoprotein MUC1 in the glycocalyx leads to a dramatic increase in the production of EVs [1]. Here we summarize our recent findings characterizing the physical properties of these mucin-induced EVs (MUC-EVs).

Summary of Research:

Extracellular vesicles (EVs) have quickly gained traction in numerous areas of biomedical engineering research — including disease pathogenesis and drug delivery, among others — due to their ability to transport DNA, RNA, and proteins. The glycocalyx is a polymer meshwork of proteins, nucleic acids, and glycans which dictates numerous intercellular interactions. However, the role of the glycocalyx in regulating intercellular communication by way of EVs remains poorly understood. It has been previously shown that engineering the glycocalyx via the overexpression of mucin can result in membrane morphologies which are favorable for the formation of EVs [1]. This report summarizes research from the last year characterizing the effects of MUC1 overexpression on EV properties.

MCF10A cells were genetically engineered to overexpress a tetracycline-inducible MUC1-construct. A single clone was then expanded and used as a workhorse cell line for this research, hereafter referred to as MCF10A-

1E7 cells. To induce MUC1 overexpression, MCF10A-1E7 cells were treated with 1 $\mu\text{g}/\text{mL}$ doxycycline (Dox) for 24 h. Uninduced MCF10A.1E7 cells were used as a negative control. Subsequently, the cells were switched to serum-free media and cultured at 37°C, 5% CO₂ for 15 h to 18 h. EV-containing media was harvested, and the EVs were isolated by PEG-enrichment [2]. EV mucin coatings were optionally removed by treatment with stcE mucinase [3], and EV sizes and concentrations were measured by nanoparticle tracking analysis (NTA) using the Malvern NS300 Nanosight.

Figure 1 shows that mucin-induced EVs (MUC-EVs) are themselves coated in MUC1. Treatment of mucin-induced EVs with StcE mucinase resulted in an overall decrease in EV size consistent with the removal of MUC1 from the EV surface [4]. The stability of MUC-EVs stored at 4°C was evaluated by repeatedly recording NTA measurements of MUC-EV samples with or without mucinase treatment over the span of seven days. Non-mucinase-treated MUC-EV stability was dramatically improved over MUC-EVs which had their MUC1 coatings cleaved by StcE mucinase, as shown in Figure 2, with only mucinase-treated EVs decaying to 50% of their original concentration within seven days. This suggests that MUC1 overexpression enhances EV stability through the generation of EVs with MUC1 surface coatings.

Recognizing the MUC1 overexpression is a hallmark of numerous solid-tumor cancers, EV production was analyzed from KPL-1, a MUC1-overexpressing breast cancer cell line. A MUC1 knockdown cell line (KPL-1 MUC1KD) was generated by lentiviral delivery of small hairpin RNA (shRNA) with reduced MUC1 expression validated by flow cytometry shown in Figure 3. EVs were harvested from wild-type KPL-1 and KPL-1 MUC1KD using the same method as described above. Figure 4 demonstrates that MUC1 knockdown dramatically attenuated the release of EVs from KPL-1 cells.

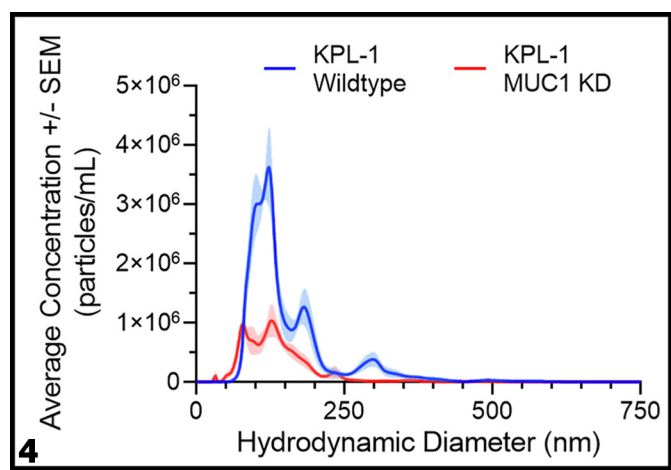
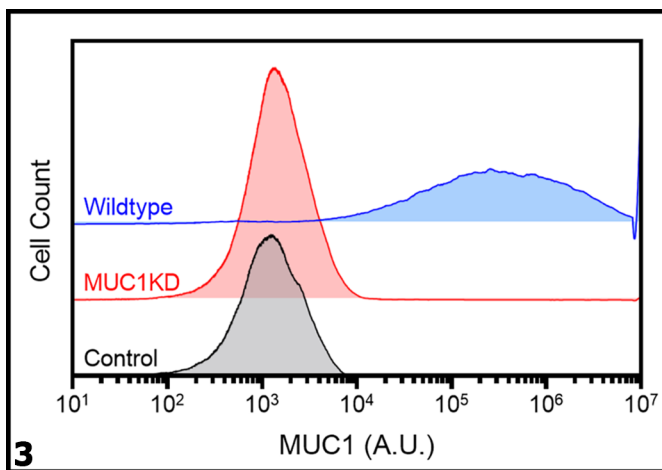
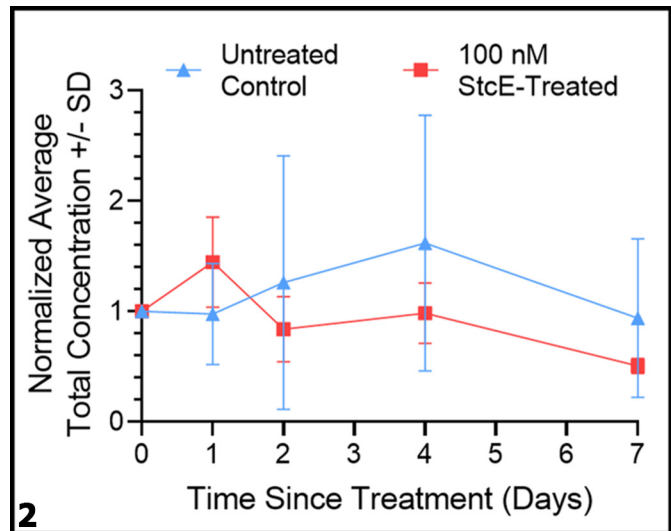
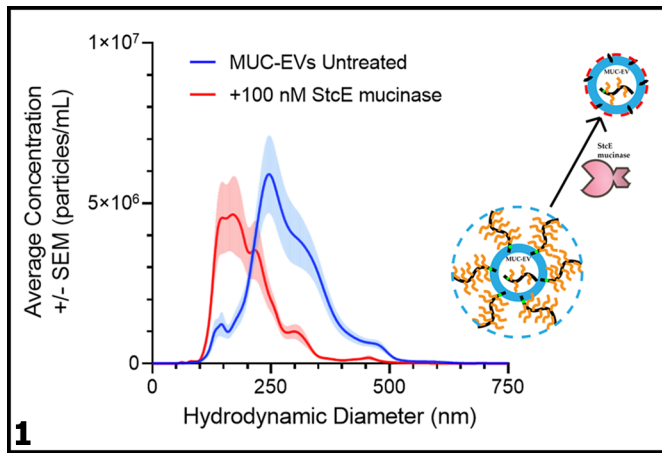


Figure 1: Induced biogenesis of MUC1-coated EVs. Size distributions of EVs from MCF10A.1E7 cells before and after 100 nM StcE mucinase treatment measured by NTA. Plotted are the average particle concentrations \pm SEM from three independent experiments.

Figure 2: MUC1 coatings improve EV stability. Total particle concentrations of EVs from MCF10A-1E7 measured by NTA. EVs were either untreated (Control) or treated with 100 nM StcE mucinase. Plotted are the average total particle concentrations \pm SD from three independent experiments as a percentage of the concentration at Day 0. Dotted line represents 50% EV decay. **Figure 3: Validation of MUC1**

knockdown in engineered KPL-1 cells. Wildtype KPL-1 and KPL-1 MUC1KD cells were fixed with 4% PFA for 15 min at room temperature, incubated with mouse anti-MUC1 (HPMV) primary antibody for 30 min at room temperature, and finally incubated with goat anti-mouse IgG secondary antibody conjugated with AlexaFluor™ 647 for 30 min at room temperature. Fluorescence histograms shown were acquired using an Attune™ NxT flow cytometer. KPL-1 wildtype cells fixed and stained only with secondary antibody were used as a negative control.

Figure 4: MUC1 knockdown attenuates release of EVs from KPL-1 breast cancer cell line. Size distributions of EVs from wildtype KPL-1 and KPL-1 MUC1KD measured by NTA. Plotted are the average particle concentrations \pm SEM from five technical replicates.

Conclusions and Future Steps:

Altogether, these data demonstrate that EV properties can be dramatically impacted by the glycocalyx. Overexpression of MUC1 acts as a driver of EV release, and these EVs may be imparted with mucin coatings which improve stability and could enhance their role as long-range delivery vehicles of therapeutic or oncogenic agents. Further studies are needed to characterize MUC-EV cargoes and to explore the applications of engineered EV mucin coatings.

References:

- [1] Shurer, C. R., et al. (2019). Physical Principles of Membrane Shape Regulation by the Glycocalyx. *Cell*, 177(7), 1757-1770. <https://doi.org/10.1016/j.cell.2019.04.017>.
- [2] Rider, M., et al. (2016). ExtraPEG: A Polyethylene Glycol-Based Method for Enrichment of Extracellular Vesicles. *Sci Rep* 6, 23978. <https://doi.org/10.1038/srep23978>.
- [3] Malaker, S.A., et al. (2019). The mucin-selective protease StcE enables molecular and functional analysis of human cancer-associated mucins. *PNAS*, 116(15), 7278-7287. <https://doi.org/10.1073/pnas.1813020116>.
- [4] Park, S., et al. (2022). Mucins form a barrier against immune cell attack. *bioRxiv*. <https://doi.org/10.1101/2022.01.28.478211>.

Fabrication and Characterization Support for CCMR

CNF Project Number: 2974-21

Principal Investigator(s): Jonathan Shu

User(s): Philip Carubia

Affiliation(s): Cornell Center for Materials Research (CCMR), Cornell University

Primary Source(s) of Research Funding: National Science Foundation

Contact: jbs24@cornell.edu, pmc228@cornell.edu

Website: www.ccmr.cornell.edu

Primary CNF Tools Used: Universal Laser Systems VersaLaser VLS3.50

Abstract:

The Cornell NanoScale Facility (CNF) is accessed for use of the Universal Laser Systems VersaLaser VLS3.50, and laser cutting 20 mm, 25 mm, and 40 mm discs from PSA backed grinding papers to be used with the DHR3 shear rheometer located in the Cornell Center for Materials Research (CCMR).

Summary of Research:

Project 2974-21 was established for facilities staff from the Cornell Center for Materials Research (CCMR) to access basic instrumentation within the Cornell NanoScale Facility (CNF) for purposes of sample preparation and fabrication of accessories for CCMR instrumentation. The initial project proposal was started to gain access to the Universal Laser Systems VersaLaser VLS3.50 by the bard materials facility for cutting 20 mm, 25 mm, and 40 mm discs from PSA backed grinding papers to be used with our DHR3 shear Rheometer. These discs are used to increase the friction between stiffer samples and the instrument to reduce artifacts related to sample slippage.

Conclusions and Future Steps:

Access to this laser cutter has allowed us to test tougher hydrogels and viscoelastic materials at higher strains than previously available. It is likely that we will be using the Universal Laser Systems VersaLaser VLS3.50 in the future as we use up our existing stock.

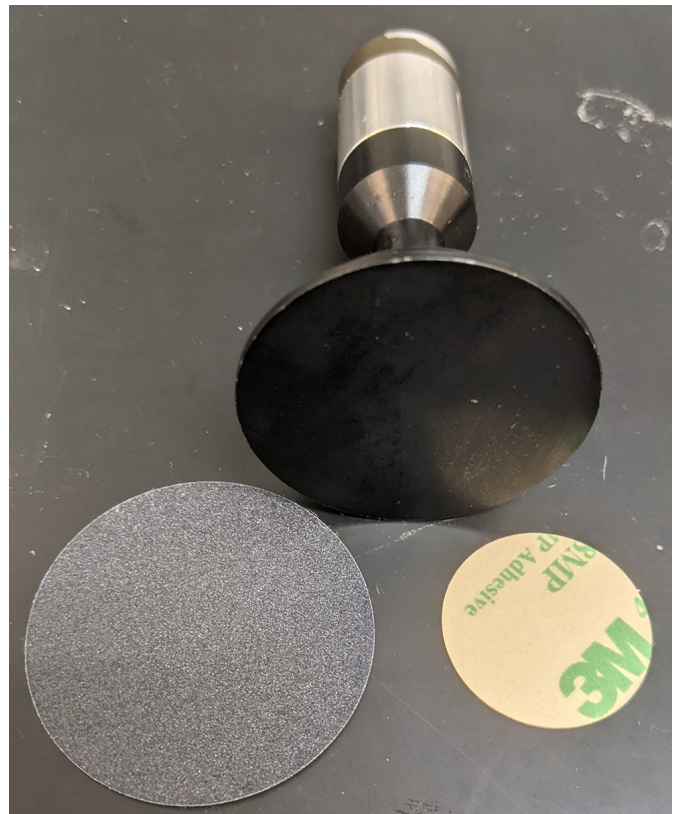


Figure 1: 40 mm upper parallel plate geometry with 40 mm disc front and 25 mm disc back.

Fabrication and RF Evaluations of 5G Antennas on Flexible Substrates

CNF Project Number: 3038-22

Principal Investigator(s): Mark D. Poliks

User(s): Dylan Richmond

Affiliation(s): Materials Science and Engineering, Binghamton University

Primary Source(s) of Research Funding: SUNY Research Foundation

Contact: mpoliks@binghamton.edu, drichmo2@binghamton.edu

Primary CNF Tools Used: Electron beam evaporator (odd & even hour),
Heidelberg Mask Writer - DWL2000, DISCO dicing saw

Abstract:

Internet-of-things (IoT) implementations are becoming increasingly popular as real-time sensing and edge computing aim to improve efficiency, safety, and wellness. To enable communication among IoT devices, such as self-driving cars, mobile, and wearable devices, they must be networked and are often reliant on rapid signal transmission and processing. Flexible glass and flexible ceramic have emerged as two primary candidates for the fabrication of high-quality roll-to-roll (R2R) antennas at low cost. We have previously demonstrated a fully additive technique for fabricating double-sided 5G Vivaldi antennas using aluminum on flexible glass [1]. This work continues and expands the scope of substrates, metallizations, and RF devices to develop wafer-level processes that can be ported to R2R. Herein, we demonstrate fabrication of double-sided 5G mm-wave RF devices on flexible glass and ceramic operating at 28 and 39 GHz. Devices are designed and simulated using ANSYS high-frequency structure simulator (HFSS). Validation of the designs is conducted by measuring the return loss and 3D radiation patterns using a Rohde and Schwarz ZNB-40 Vector Network Analyzer (VNA) and comparing operational performance to simulated results. While a R2R manufacturing process is developed in tandem, the wafer scale prototypes have been made using standard materials, processes, and facilities to allow a facile translation to R2R.

Summary of Research:

RF devices were fabricated on flexible glass and ceramic wafers using both conventional photolithography and depositions with shadow masks to define features. First, metals were evaporated onto both sides of the wafer substrates using the electron beam evaporators available in the CNF. Blank photomasks were purchased from the CNF store and designs were exposed using the direct-write expose tool to define mask patterns. Photolithography was performed at Binghamton University's clean room on the

wafers metallized at the CNF. Once metal patterns were defined onto the wafer, a subsequent via filling process was done to make electrical connections from one side of the wafer to the other. Wafers were then coated in a dry film photoresist and brought back to the CNF for dicing. The DISCO dicing saw was used (with the all-purpose blade) to singulate the devices from the wafer. Finally, devices were evaluated for their RF performance using a vector network analyzer to obtain S-parameters and radiation patterns in an anechoic chamber.

Conclusions and Future Steps:

This work was meant to prototype and evaluate processes that can be used to fabricate these devices on webs of flexible materials on a larger scale, roll-to-roll (R2R) manufacturing level. The initial trails of fabricating these devices were successful in that the devices operated as expected. The next steps consist of testing the compatibility of these webs of flexible materials with our tool set at Binghamton University and begin to carry out preliminary experiments on the R2R platform towards high-volume manufacturing these devices. The final step will eventually be the manufacturing of these devices.

References:

- [1] M. D. Poliks, et al., "Transparent antennas for wireless systems based on patterned indium tin oxide and flexible glass," in 2017 IEEE 67th Electronic Components and Technology Conference (ECTC), 2017, pp. 1443-1448.
- [2] J. P. Lombardi, et al., "Copper transparent antennas on flexible glass by subtractive and semi-additive fabrication for automotive applications," in 2018 IEEE 68th Electronic Components and Technology Conference (ECTC), 2018, pp. 2107-2115.
- [3] D. Richmond, et al. "Additive Fabrication of Aluminum Antennas on Flexible Glass," New York State Nanotechnology Network (NNN) Symposium, May 2022.
- [4] D. Richmond, et al. "Fabrication and RF evaluations of 5G Antennas on Flexible Substrates," New York State Nanotechnology Network (NNN) Symposium, April 2023.

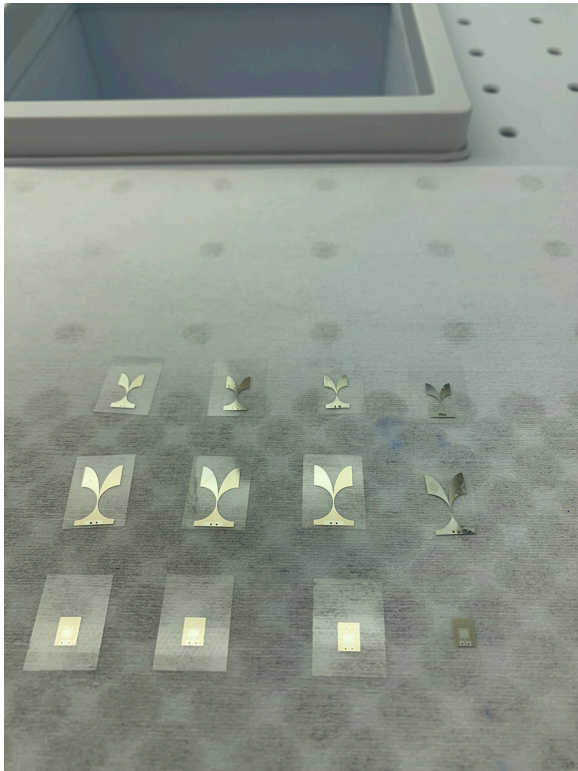


Figure 1: RF devices on 100 μm flexible glass, diced using DISCO dicing saw.

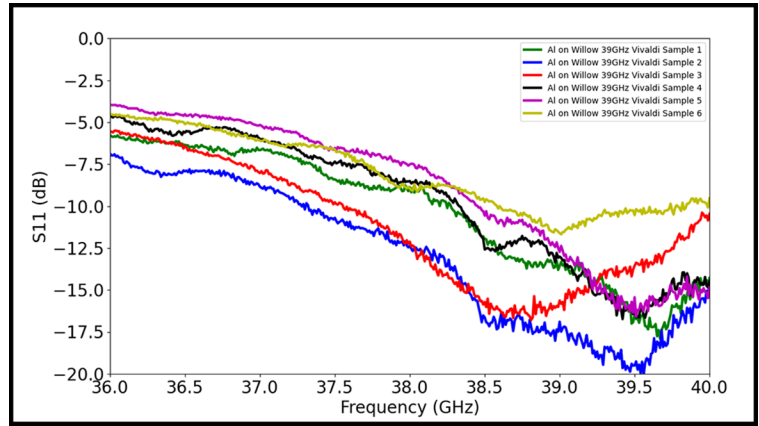


Figure 2: Return loss (S11) of Vivaldi antennas on 100 μm flexible glass.

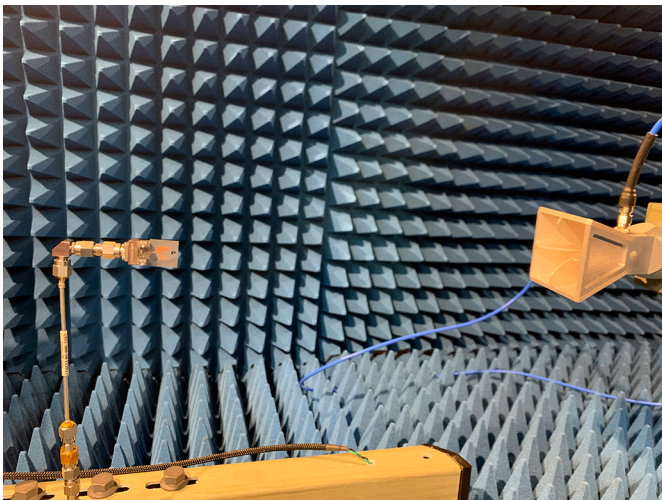


Figure 3: Anechoic chamber radiation measurement setup.

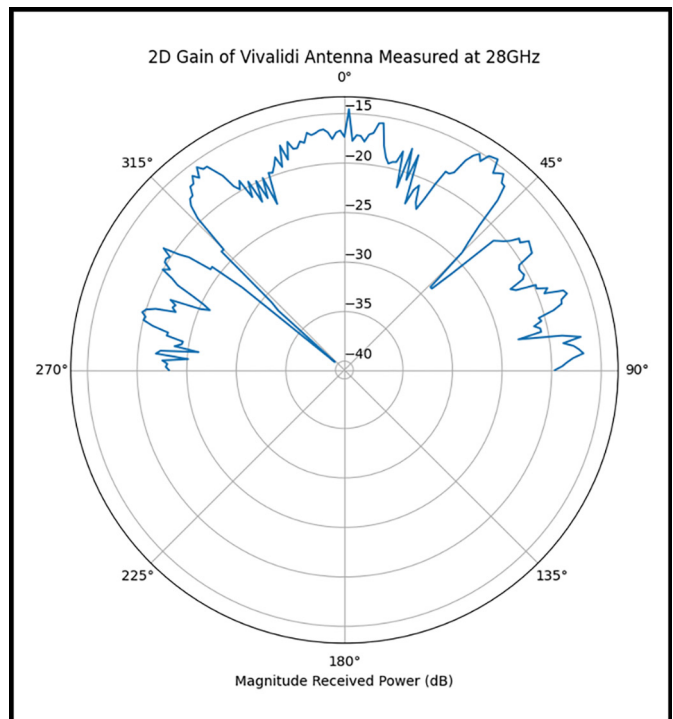


Figure 4: 2D gain of Vivaldi antenna on 40 μm flexible ceramic measured at 28 GHz.

Wolfspeed Development of T-Gate Structure by Electron Beam Lithography

CNF Project Number: 3073-23

Principal Investigator(s): Evan Jones

User(s): Evan Jones, Jim Tajadod

Affiliation(s): Wolfspeed, Inc.

Primary Source(s) of Research Funding: Internal Research and Development

Contact: Evan.Jones@wolfspeed.com, Jim.Tajadod@wolfspeed.com

Primary CNF Tools Used: JEOL 9500

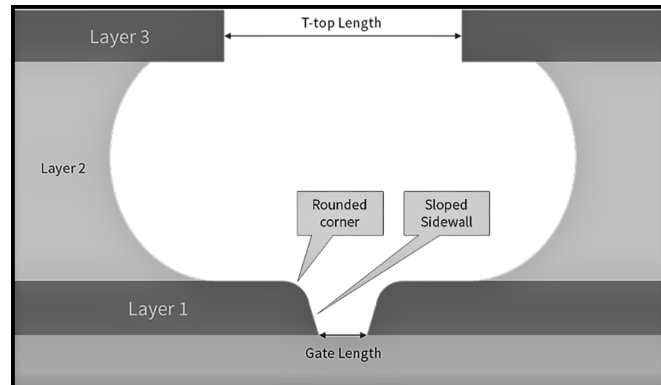


Figure 1: Schematic of target cross section.

Abstract:

Wolfspeed aims to add electron-beam lithography (EBL) processes to our toolset to improve our competitive position in the RF electronics markets.

Summary of Research:

Near term goals to be accomplished at Cornell NanoScale Facility (CNF) over a time range of 12 to 24 months include gain experience in EBL, identify baseline functional process for transfer into NC Fabrication upon toolset installation, and identify EBL toolset and facility specifications based on development work. Prototype demonstration of fully functional “T-Gate” HEMT 90 nm gate length with 30 nm overlay on 100 mm wafer processing. Long term goals to be accomplished beyond work at CNF include fully outfit EBL toolset, transfer process knowledge into NC Fab, and fully staff EBL process organization. A schematic of the target “T-Gate” profile is shown in Figure 1.

Conclusions and Future Steps:

Work was initiated in the summer of 2023.

References:

- [1] Chen, Y., et al. “T-Gate Fabrication Using a ZEP520A/UVIII Bilayer.” *Microelectronic Engineering*, vol. 57-58, 2001, pp. 939-943., [https://doi.org/10.1016/s0167-9317\(01\)00475-0](https://doi.org/10.1016/s0167-9317(01)00475-0).
- [2] Kim, Tae-Woo, et al. “Effect of a Two-Step Recess Process Using Atomic Layer Etching on the Performance of $\text{In}_{0.52}\text{Al}_{0.48}\text{As}/\text{In}_{0.53}\text{Ga}_{0.47}\text{As}$ P-HEMTs.” *IEEE Electron Device Letters*, vol. 28, no. 12, 2007, pp. 1086-1088., <https://doi.org/10.1109/led.2007.910278>.
- [3] Ocola, Leonidas E., and Aaron Stein. “From Microchannels to Nanochannels in a Bilayer Resist.” *Nanofabrication: Technologies, Devices, and Applications*, 2005, <https://doi.org/10.1117/12.572068>.
- [4] Zhong, Yinghui, et al. “T.Gate Fabrication of Inp-Based HEMTs Using PMGI/ZEP520A/PMGI/ZEP520A Stacked Resist.” *Chinese Journal of Electronics*, vol. 25, no. 3, 2016, pp. 448-452., <https://doi.org/10.1049/cje.2016.05.009>.
- [5] Zhu, Mingsai, et al. “Nanofabrication of T Shape Gates for High Electron Mobility Transistors in Microwaves and THz Waves, a Review.” *Micro and Nano Engineering*, vol. 13, 2021, p. 100091., <https://doi.org/10.1016/j.mne.2021.100091>.
- [6] Fitch, Walker, et al. “Implementation of High-Power-Density X-Band AlGaIn/GaN High Electron Mobility Transistors in a Millimeter-Wave Monolithic Microwave Integrated Circuit Process” *IEEE Electron Device Letters*, Vol. 36, No. 10, October 2015.